IRS-Aided SWIPT: Joint Waveform, Active and Passive Beamforming Design

Yang Zhao, *Member, IEEE,* Bruno Clerckx, *Senior Member, IEEE* and Zhenyuan Feng, *Member, IEEE*

***Abstract*—The performance of Simultaneous Wireless Information and Power Transfer (SWIPT) is mainly restricted by the strength of the received Radio-Frequency (RF) signal. To tackle this problem, we introduce a low-power Intelligent Reflecting Surface (IRS) that compensates the propagation loss and boosts the energy efficiency with a passive beamforming gain. This paper investigates an IRS-aided Orthogonal Frequency Division Multiplexing (OFDM) SWIPT system based on a practical nonlinear energy harvester model, where a multi-antenna Access Point (AP) transmits information and energy simultaneously to a single-antenna user under the assist of IRS. We aim to maximize the Rate-Energy (R-E) region through a joint optimization of the transmit waveform and active beamforming at the AP, the reflection coefficients at the IRS, and the power splitting ratio at the user. The performance of the proposed design is compared with those of no IRS, non-adaptive (information-optimized, power-optimized) IRS and ideal Frequency-Selective (FS) IRS, and we confirm that due to rectifier nonlinearity, a dedicated power signal can be beneficial to energy harvesting (EH). It has the consequence that the Time-Switching (TS) receiver is preferred over Power-Splitting (PS) receiver for multi-carrier transmission at a low Signal-to-Noise Ratio (SNR). Simulation results demonstrate that the proposed design based on a joint waveform, active and passive beamforming optimization brings effective R-E enhancement over benchmark schemes for broadband transmission, and the optimal IRS can be approximated in closed form with negligible performance loss for single transmit antenna narrowband SWIPT.**

***Index Terms*—Wireless information and power transfer, intelligent reflecting surface, waveform design, active and passive beamforming.**

I. Introduction

A. Simultaneous Wireless Information and Power Transfer

With the great advance in communication performance, a bottleneck of wireless networks comes to energy supply. Most existing mobile devices are powered by batteries that require frequent charging or replacement, which causes high maintenance cost and restricts the scale of networks. Although solar energy and inductive coupling have become popular alternatives, the former depends on the environment while the latter has a very short operation range. Simultaneous Wireless Information and Power Transfer (SWIPT) is a promising solution to connect and power mobile devices via electromagnetic (EM) waves in the Radio-Frequency (RF) band. It provides low power at μW level but broad coverage up to hundreds of meters in a sustainable and controllable manner, bringing more opportunities to the Internet of Things (IoT) and Machine to Machine (M2M) networks. The upsurge in the number of connected devices, together with the decreasing trend in the power consumption of electronics, call for a rethinking of future wireless networks based on Wireless Power Transfer (WPT) and SWIPT [1].

The concept of SWIPT was first cast in [2], where the authors investigated the Rate-Energy (R-E) tradeoff for a flat Gaussian channel and typical discrete channels. Two co-localized information and power receivers were then proposed in [3], namely Time Switching (TS) that switches between Energy Harvesting (EH) and Information Decoding (ID) modes, and Power Splitting (PS) that splits the received signal into individual components. Dedicated information and energy beamforming were then investigated in [4], [5] to characterize the R-E region for multi-antenna broadcast and interference channels. On the other hand, [6] pointed out that the Radio Frequency-to-Direct Current (RF-to-DC) conversion efficiency depends on the rectifier input power level. It implies that the modeling of the energy harvester, in particular its nonlinearity, has a crucial and significant impact on the waveform preference, resource allocation and system design of any wireless-powered systems [1], [6], [7]. Motivated by this, [8] derived a tractable nonlinear harvester model based on the Taylor expansion of diode I-V characteristics, then implemented joint waveform and beamforming design for WPT. Simulation and experiments demonstrated the inaccuracy of the rectenna linear model and emphasized the benefit of modeling the rectifier nonlinearity in real system design [9], [10]. Importantly, the joint waveform and beamforming strategy for WPT was also shown experimentally in [11] to be a key technique to expand operation range. The work was extended to SWIPT in [12]. Uniquely, it showed that the rectifier nonlinearity leads to radical changes to SWIPT design, namely 1) modulated and unmodulated waveforms are not equally suitable for wireless power delivery; 2) a multicarrier unmodulated waveform superposed to a multicarrier modulated waveform is useful to enlarge the R-E region of SWIPT; 3) a combination of power splitting and time sharing is in general the best strategy; 4) the optimal input distribution is not the conventional Circularly Symmetric Complex Gaussian (CSCG); 5) the rectifier nonlinearity is beneficial to system performance and is essential to efficient SWIPT design. Those observations, validated experimentally in [9], led to the question "what is the optimal input distribution for SWIPT under nonlinearity?". This question was answered in [13] for single-carrier SWIPT, and some attempts were further made in [14] for multi-carrier SWIPT. The answer sheds new light to fundamental limits of SWIPT and practical signaling (e.g. modulation and waveform) strategies. It is now

The authors are with the Department of Electrical and Electronic Engineering, Imperial College London, London SW7 2AZ, U.K. (e-mail: yang.zhao18@imperial.ac.uk; b.clerckx@imperial.ac.uk).

well understood from [12]–[14] that, due to the nonlinearity, a combination of CSCG and On-Off Keying in single-carrier setting and non-zero mean and asymmetric inputs in multi-carrier setting lead to significantly larger R-E region compared to conventional CSCG. Recently, [15] used machine learning techniques to design SWIPT signaling under nonlinearity to complement the information theoretic results of [13] and new modulation schemes were subsequently designed.

B. Intelligent Reflecting Surface

Intelligent Reflecting Surface (IRS) has recently emerged as a promising technique that adapts the wireless channel to increase spectrum and energy efficiency. In practice, an IRS consists of multiple individual reflecting elements that adjust the amplitude and phase of the incident signal through passive beamforming. Different from relay and backscatter, IRS assists the primary transmission using fully passive components, thus consumes less power with no additional thermal noise but is limited to frequency-flat (FF) reflection. Although Frequency-Selective Surface (FSS) has received much attention for wideband communications, it is different from IRS as active FSS requires RF-chains [16] while passive FSS has fixed physical characteristics and is non-adaptive [17].

Inspired by the development of real-time reconfigurable metamaterials [18], the authors of [19] introduced a programmable metasurface that steers or polarizes the EM wave at specific frequency to mitigate signal attenuation. Motivated by this, [20] proposed an IRS-assisted Multiple-Input Single-Output (MISO) system and jointly optimized the precoder at the Access Point (AP) and the phase shifts at the IRS to minimize the transmit power. The active and passive beamforming problem was extended to the discrete phase shift case [21] and the multiuser case [22]. Starting from the impedance equation, [23] investigated the influence of phase shift on the reflection amplitude and proposed a parametric IRS model via curve fitting. In [24], channel estimation for Time-Division Duplex (TDD) systems was carried through a two-stage Minimum Mean Squared Error (MMSE)-based protocol that sequentially estimates the cascaded channel through each reflector with the others switched off. To reduce estimation overhead and design complexity, [25] exploited the spatial correlation and proposed a group-based IRS model where adjacent elements share a common reflection coefficient. Recent research also explored the possibility of integrating IRS into Orthogonal Frequency-Division Multiplexing (OFDM) systems. For example, [26] further enhances time diversity by dynamic passive beamforming that varies IRS over consequent time slots, which enables flexible resource allocation over time-frequency Resource Blocks (RBs). In [27], a prototype IRS with 256 2-bit elements based on Positive Intrinsic-Negative (PIN) diodes was developed to support real-time high-definition video transmission at GHz and mmWave frequency.

C. IRS-aided SWIPT

The effective channel enhancement and low power consumption of IRS are expected to bring more opportunities to SWIPT. It was argued in [28] that dedicated energy beam is power-inefficient and may cause interference, thus not required to maximize the Weighted Sum-Power (WSP) for a multiuser IRS-assisted SWIPT system. On the other hand, [29] suggested that if the interference can be cancelled, multiple energy beams are generally required for the max-min harvested power problem. [30] proposed a novel penalty-based algorithm, whose inner layer employs Block Coordinate Descent (BCD) method to update transmit precoders and IRS phase shifts while the outer layer updates the penalty coefficients. It demonstrated that Line-of-Sight (LoS) links can boost the harvested power because the rank-deficient channels are highly correlated. In such cases, a single energy stream is enough for all energy receivers.

However, to the best of the authors' knowledge, all existing IRS-assisted SWIPT papers focus on single-carrier transmission based on an oversimplified linear harvester model for separated information and energy receivers. Rectifier nonlinearity and co-localized receiver, acknowledged as key to practical and efficient SWIPT system design, have not yet been addressed in the relevant research. In this paper, we marry the benefits of joint waveform and active beamforming optimization for SWIPT (accounting for nonlinearity) with the passive beamforming capability of IRS. The contribution of the paper are listed as follows.

First, we introduce an novel IRS-aided SWIPT architecture based on a joint waveform, active and passive beamforming design. This architecture can be seen to IRS-aided SWIPT what [12] is to SWIPT. Specifically, we consider a multi-carrier IRS-aided downlink MISO SWIPT system where the IRS assists the information and energy transmission to a single user. A multicarrier unmodulated power waveform (deterministic multisine) is superposed to a multicarrier modulated information waveform to boost the energy transfer efficiency. The power and information waveforms and active beamforming at the transmitter, the phase shifts at the IRS and the splitting ratio at the receiver are jointly optimized to maximize the R-E tradeoff while accounting for the rectenna nonlinearity. This is the first paper to proposed such a joint waveform, active and passive beamforming architecture for IRS-aided SWIPT. Note that existing IRS-aided SWIPT papers [28]–[31] focus on single-carrier transmissions and ignore the rectenna nonlinearity (and therefore assume the oversimplified and inaccurate linear model), which prevents from exploiting the waveform gain in SWIPT system design. On the contrary, this paper focus on multicarrier IRS-SWIPT and investigates the fundamental impact of harvester nonlinearity on joint waveform, active and passive beamforming design.

Second, we formulate an optimization for this joint waveform, active and passive beamforming design so as to characterize the R-E region achieved by the proposed architecture. The R-E region characterization problem is transformed into multiple energy maximization problems subject to different rate constraints. Each achievable R-E pair is obtained through an Alternating Optimization (AO) algorithm that iteratively updates 1) phase shift at the IRS 2) waveform and active beamforming at the transmitter, power splitting ratio at the receiver, until convergence. On top of the SWIPT optimization based on Geometric Programming (GP) [12], our IRS-aided SWIPT

optimization employs an low-complexity passive beamforming algorithm based on Successive Convex Approximation (SCA) and Semidefinite Relaxation (SDR), which solves the highly non-convex problem in a efficient and reliable manner. Despite no rigorous mathematical proof exists for the convergence of the relaxed IRS phase shift problem, numerical results demonstrated SDR is tight and the proposed algorithm can always find a stationary point for all tested channel realizations under different configurations.

Third, we conduct numerical evaluations that demonstrate the benefit of the proposed architecture. It is demonstrated that the observations for SWIPT carries on to IRS-aided SWIPT. For example, dedicated power waveform can boost the energy transmission efficiency for multi-carrier transmission, and TS and PS are preferred at low and high SNR, respectively. Results also confirmed that the IRS bring a significant channel amplification and R-E enhancement with no impact on the waveform preference and transceiving strategy. In contrast to the active amplify-and-forward relay whose optimal location is around the midpoint [32], we observed that the passive IRS should be placed next to either the transmitter or the receiver to further improve the R-E tradeoff, due to the product-distance path loss model. It implies that that equipping the AP with an IRS can effectively extend the operation range of SWIPT systems. Also, the adaptive IRS design outperformed the fixed (information-optimized, power-optimized) IRS for broadband transmission, and the optimal IRS can be approximated in closed form for single transmit antenna narrowband SWIPT.

Organization: The rest of this paper is organized as follows. Section II introduces the signal, channel, receiver and R-E tradeoff models of the IRS-aided SWIPT system. Section III tackles the waveform, active and passive beamforming optimization. Section IV presents simulation results to evaluate the proposed design. Section [TODO] concludes the paper.

Notations: Scalars are denoted by italic letters, vectors are denoted by bold lower-case letters, and matrices are denoted by bold upper-case letters. j refers to the imaginary unit. $\mathbb{C}^{x\times y}$ denotes the subspace spanned by complex $x\times y$ matrices. $\Re\{\cdot\}$ and $\Im\{\cdot\}$ stand for the real and imaginary part of a complex number or variable, respectively. $(\cdot)^*$, $(\cdot)^T$ and $(\cdot)^H$ represent the conjugate, transpose, and conjugate transpose operators, respectively. $\mathcal{A}\{\cdot\}$ extracts the DC component of a signal, and $\mathcal{E}_X\{\cdot\}$ takes the expectation over the distribution of the random variable X (X may be omitted for simplicity). For a scalar x, $|x|$ denotes its absolute value. For a vector $\boldsymbol{x}$, $\|\boldsymbol{x}\|$ refers to its Euclidean norm, $\arg(\boldsymbol{x})$ refers to its argument vector, and $\mathrm{diag}(\boldsymbol{x})$ refers to a square diagonal matrix with the elements of $\boldsymbol{x}$ on the main diagonal. For a general matrix $\boldsymbol{M}$, $\mathrm{rank}(\boldsymbol{M})$ denotes it rank. For a square matrix S, $\mathrm{Tr}(\boldsymbol{S})$ denotes its trace, and $\boldsymbol{S}\succeq 0$ means that $\boldsymbol{S}$ is positive semi-definite. The distribution of a random vector consists of Circularly Symmetric Complex Gaussian (CSCG) variables is denoted by $\mathcal{CN}(\boldsymbol{\mu},\boldsymbol{\Sigma})$, where $\boldsymbol{\mu}$ is the mean vector and $\boldsymbol{\Sigma}$ is the covariance matrix. $\sim$ means "distributed as". We also denote $(\cdot)^\star$ and $(\cdot)^{(i)}$ as stationary solution and solution at iteration i, respectively.

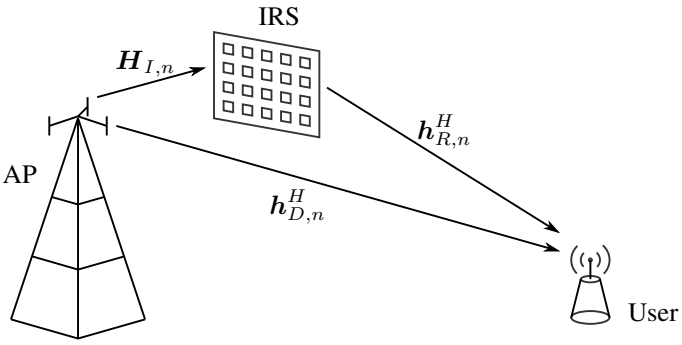

Fig. 1. An IRS-aided OFDM SWIPT system.

II. System Model

As shown in Fig. 1, we consider an IRS-aided SWIPT system where a M-antenna AP delivers information and power simultaneously, through a L-reflector IRS, to a single-antenna user over N orthogonal evenly-spaced subbands with center frequency f_n ($n=1,\ldots,N$). Perfect Channel State Information (CSI) at the transmitter, IRS and receiver with negligible training overhead are assumed to explore the upper bound of the proposed design. A quasi-static block fading channel model is considered for all links, and we focus on one particular block where the channels are approximately unchanged. Two practical co-located receiver architectures are compared in terms of R-E region. Specifically, TS divides each time slot into orthogonal data and energy slots and performs a time sharing between WPT and Wireless Information Transfer (WIT). In comparison, PS splits the received signal into individual ID and EH streams such that the splitting ratio ρ is coupled with waveform and IRS design. Perfect synchronization is assumed among the three parties in both scenarios, and signals reflected by IRS for two and more times are omitted. We also assume the noise power is too small to be harvested.

A. Transmit Signal

Denote $\tilde{x}_{I,n}(t)$ as the information symbol transmitted over subband n, which follows an i.i.d. CSCG distribution with zero mean and unit variance, namely $\tilde{x}_{I,n}\sim\mathcal{CN}(0,1)$. The superposed transmit signal on antenna m ($m=1,\ldots,M$) at time t is

$$x_m(t)=\Re\left\{\sum_{n=1}^{N}\left(w_{I,n,m}\tilde{x}_{I,n}(t)+w_{P,n,m}\right)e^{j2\pi f_n t}\right\} \quad (1)$$

where $w_{I/P,n,m}$ denotes the weight of the information and power signal transmitted by antenna m at subband n. Define $\boldsymbol{w}_{I/P,n}=[w_{I/P,n,1},\ldots,w_{I/P,n,M}]^T\in\mathbb{C}^{M\times 1}$ by stacking up weights across all antennas. Therefore, the transmit information and power signals write as

$$\boldsymbol{x}_I(t)=\Re\left\{\sum_{n=1}^{N}\boldsymbol{w}_{I,n}\tilde{x}_{I,n}(t)e^{j2\pi f_n t}\right\}, \quad (2)$$

$$\boldsymbol{x}_P(t)=\Re\left\{\sum_{n=1}^{N}\boldsymbol{w}_{P,n}e^{j2\pi f_n t}\right\}. \quad (3)$$

B. Composite Channel

At subband n, denote the AP-user direct channel as $\boldsymbol{h}_{D,n}^H \in \mathbb{C}^{1\times M}$, AP-IRS incident channel as $\boldsymbol{H}_{I,n} \in \mathbb{C}^{L\times M}$, and IRS-user reflective channel as $\boldsymbol{h}_{R,n}^H \in \mathbb{C}^{1\times L}$. At the IRS, element l ($l = 1, \ldots, L$) redistributes the incoming signal by adjusting the reflection amplitude $\gamma_l \in [0, 1]$ and phase shift $\theta_l \in [0, 2\pi)$ [1]. Define the IRS matrix as $\boldsymbol{\Theta} = \mathrm{diag}(\gamma_1 e^{j\theta_1}, \ldots, \gamma_L e^{j\theta_L}) \in \mathbb{C}^{L\times L}$ that collects the reflection coefficients onto its main diagonal entries. The extra link introduced by IRS can be modeled as a concatenation of the AP-IRS incident channel, IRS reflection matrix, and IRS-user reflective channel. On top of this, the total composite channel is obtained by superposing the IRS-aided extra channel to the AP-user direct channel as

$$\boldsymbol{h}_n^H = \boldsymbol{h}_{D,n}^H + \boldsymbol{h}_{R,n}^H \boldsymbol{\Theta} \boldsymbol{H}_{I,n} = \boldsymbol{h}_{D,n}^H + \boldsymbol{\phi}^H \boldsymbol{V}_n \tag{4}$$

where $\boldsymbol{\phi} = [\gamma_1 e^{j\theta_1}, \ldots, \gamma_L e^{j\theta_L}]^H \in \mathbb{C}^{L\times 1}$ and $\boldsymbol{V}_n = \mathrm{diag}(\boldsymbol{h}_{R,n}^H)\boldsymbol{H}_{I,n} \in \mathbb{C}^{L\times M}$. Note the conjugate transpose in the notation of $\boldsymbol{\phi}$ makes its entries the complex conjugate of the diagonal entries of $\boldsymbol{\Theta}$.

C. Receive Signal

At the single-antenna receiver, the total received signal $y(t) = y_I(t) + y_P(t)$ captures the contribution from information and power components over N subbands, where

$$y_I(t) = \Re\left\{ \sum_{n=1}^{N} \boldsymbol{h}_n^H \boldsymbol{w}_{I,n} \tilde{x}_{I,n}(t) e^{j2\pi f_n t} \right\}, \tag{5}$$

$$y_P(t) = \Re\left\{ \sum_{n=1}^{N} \boldsymbol{h}_n^H \boldsymbol{w}_{P,n} e^{j2\pi f_n t} \right\}. \tag{6}$$

D. Information Decoder

A major benefit of the superposed waveform is that the multisine power waveform creates no interference to the information waveform. Therefore, the achievable rate writes as

$$R(\boldsymbol{\phi}, \boldsymbol{w}_I, \rho) = \sum_{n=1}^{N} \log_2\left(1 + \frac{(1-\rho)|\boldsymbol{h}_n^H \boldsymbol{w}_{I,n}|^2}{\sigma_n^2}\right) \tag{7}$$

where ρ is the power splitting ratio for the energy harvester, σ_n^2 is the variance of the total noise (RF-band and RF-to-baseband conversion) on tone n. Rate 7 is achievable with either waveform cancellation or translated demodulation [12].

E. Energy Harvester

In this section, we briefly revisit a tractable nonlinear rectenna model that relates the harvester output DC current to the received waveform [8], [12]. Fig. 2a illustrates the equivalent circuit of a lossless antenna, where the incoming signal creates an voltage source $v_s(t)$ and the antenna has an impedance R_{ant}. Let R_{in} be the total input impedance of the rectifier and matching network, and we assume the voltage across matching network is negligible. When perfectly matched ($R_{\text{in}} = R_{\text{ant}}$), the rectifier input voltage is $v_{\text{in}}(t) = y(t)\sqrt{\rho R_{\text{ant}}}$.

[1]To investigate the performance upper bound of IRS, we suppose the reflection coefficient is maximized $\gamma_l = 1, \forall l$ while the phase shift is a continuous variable over $[0, 2\pi)$.

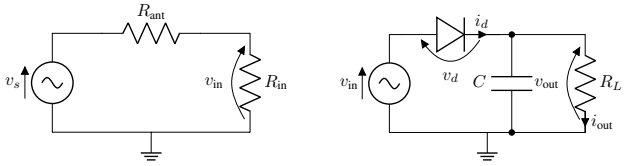

(a) Antenna equivalent circuit (b) A single diode rectifier

Fig. 2. Rectenna circuits.

Rectifiers consist of nonlinear components as diode and capacitor to produce DC output and store energy [33], [34]. Consider a simplified rectifier in Fig. 2b where a single series diode is followed by a low-pass filter with a parallel load. Denote i_s as the reverse bias saturation current, n' as the diode ideality factor, v_t as the thermal voltage, $v_d(t) = v_{\text{in}}(t) - v_{\text{out}}(t)$ as the voltage across the diode where $v_{\text{out}}(t)$ is the output voltage across the load. A Taylor expansion of the diode characteristic equation $i_d(t) = i_s(e^{v_d(t)/n'v_t} - 1)$ around a quiescent operating point a writes as $i_d(t) = \sum_{i=0}^{\infty} k_i'(v_d(t) - a)^i$, where $k_0' = i_s(e^{a/n'v_t} - 1)$ and $k_i' = i_s e^{a/n'v_t}/i!(n'v_t)^i$ for $i = 1, \ldots, \infty$. Note that this small-signal expansion model is only valid for the non-linear operation region, and the I-V relationship would be linear if the diode behavior is dominated by the load [8]. Also, an ideal low-pass filter with steady-state response can provide a constant v_{out} that depends on the peak of $v_{\text{in}}(t)$ [35]. Therefore, a proper choice of the operating voltage drop is $a = \mathcal{E}\{v_d(t)\} = -v_{\text{out}}$ such that

$$i_d(t) = \sum_{i=0}^{\infty} k_i' \rho^{i/2} R_{\text{ant}}^{i/2} y(t)^i. \tag{8}$$

By discarding the non-DC components, taking expectation over symbol distribution, and truncating 8 to the n_0-th order, we approximate the average output DC current for a given channel as

$$i_{\text{out}}(t) = \mathcal{A}\{i_d(t)\} \approx \sum_{i=0}^{n_0} k_i' \rho^{i/2} R_{\text{ant}}^{i/2} \mathcal{E}\left\{\mathcal{A}\left\{y(t)^i\right\}\right\}. \tag{9}$$

With the assumption of evenly-spaced frequencies, it holds that $\mathcal{A}\left\{y(t)^i\right\} = 0$ for odd i thus the related terms have no contribution to DC output. However, k_i' is still a function of i_{out}, and [8] proved that maximizing a truncated i_{out} is equivalent to maximizing a monotonic function

$$z(\boldsymbol{\phi}, \boldsymbol{w}_I, \boldsymbol{w}_P, \rho) = \sum_{i\,\text{even}, i\geq 2}^{n_0} k_i \rho^{i/2} R_{\text{ant}}^{i/2} \mathcal{E}\left\{\mathcal{A}\left\{y(t)^i\right\}\right\} \tag{10}$$

where $k_i = i_s/i!(nv_t)^i$. It can be observed that the traditional linear harvester model, where the output DC power equals the sum of the power harvested on each frequency, is a special case of 10 with $n_0 = 2$. However, due to the coupling among different frequencies, some high-order AC components compensate each other and further contribute to the output DC power. In other words, even-order terms with $i \geq 4$ account for the nonlinear behavior of the diode. For simplicity, we let $\beta_2 = k_2 R_{\text{ant}}$, $\beta_4 = k_4 R_{\text{ant}}^2$ and choose $n_0 = 4$ to investigate fundamental nonlinearity. Note that $\mathcal{E}\left\{|\tilde{x}_{I,n}|^2\right\} = 1$

but $\mathcal{E}\left\{|\tilde{x}_{I,n}|^4\right\}=2$, which can be interpreted as a modulation gain on the nonlinear terms of the output DC current. The corresponding z is detailed in 11.

Inspired by [36], we stack up channel and waveform vectors over all subbands as $\boldsymbol{h}=[\boldsymbol{h}_1^H,\ldots,\boldsymbol{h}_N^H]^H\in\mathbb{C}^{MN\times 1}$, $\boldsymbol{w}_{I/P}=[\boldsymbol{w}_{I/P,1}^H,\ldots,\boldsymbol{w}_{I/P,N}^H]^H\in\mathbb{C}^{MN\times 1}$. Moreover, define $\boldsymbol{W}_{I/P}=\boldsymbol{w}_{I/P}\boldsymbol{w}_{I/P}^H$ and let $\boldsymbol{W}_{I/P,n}$ keep its n-th ($n=-N+1,\ldots,N-1$) block diagonal and null the remaining entries, where the blocks are of size $M\times M$. On top of this, relevant DC terms are expressed in 12 – 15.

F. Rate-Energy Region

The achievable R-E region is defined as

$$C_{R_{\text{ID}}-I_{\text{EH}}}(P)\triangleq\Bigg\{(R_{\text{ID}},I_{\text{EH}}):R_{\text{ID}}\le R,I_{\text{EH}}\le z,\\ \frac{1}{2}\left(\|\boldsymbol{w}_I\|^2+\|\boldsymbol{w}_P\|^2\right)\le P\Bigg\}\tag{16}$$

where P is the average transmit power budget and the coefficient $1/2$ converts the peak power of sine waves to the average power.

III. Problem Formulation

We characterize the R-E region through a current maximization problem subject to transmit power, IRS magnitude, and different rate constraints

$$\begin{aligned}\max_{\boldsymbol{\phi},\boldsymbol{w}_I,\boldsymbol{w}_P,\rho}\quad & z(\boldsymbol{\phi},\boldsymbol{w}_I,\boldsymbol{w}_P,\rho) && (17a)\\ \text{s.t.}\quad & \frac{1}{2}\left(\|\boldsymbol{w}_I\|^2+\|\boldsymbol{w}_P\|^2\right)\le P, && (17b)\\ & R(\boldsymbol{\phi},\boldsymbol{w}_I,\rho)\ge\bar{R}, && (17c)\\ & |\phi_l|=1,\quad l=1,\ldots,L, && (17d)\\ & 0\le\rho\le 1\,. && (17e)\end{aligned}$$

Problem 17 is intricate due to the non-convex objective function 17a and the rate constraint 17c with coupled variables. To reduce the design complexity, we propose a suboptimal AO algorithm that iteratively updates the phase shift at the IRS, the waveform and active beamforming at the transmitter, and the power splitting ratio at the receiver, until convergence.

A. IRS Phase Shift

In this section, the IRS phase shift $\boldsymbol{\phi}$ is optimized for any given waveform $\boldsymbol{w}_{I/P}$ and splitting ratio ρ. We observe that

$$\begin{aligned}|\boldsymbol{h}_n^H\boldsymbol{w}_{I,n}|^2&=\boldsymbol{w}_{I,n}^H\boldsymbol{h}_n\boldsymbol{h}_n^H\boldsymbol{w}_{I,n}\\&=\boldsymbol{w}_{I,n}^H(\boldsymbol{h}_{D,n}+\boldsymbol{V}_n^H\boldsymbol{\phi})(\boldsymbol{h}_{D,n}^H+\boldsymbol{\phi}^H\boldsymbol{V}_n)\boldsymbol{w}_{I,n}\\&=\boldsymbol{w}_{I,n}^H\boldsymbol{M}_n^H\boldsymbol{\Phi}\boldsymbol{M}_n\boldsymbol{w}_{I,n}\\&=\mathrm{Tr}(\boldsymbol{M}_n\boldsymbol{w}_{I,n}\boldsymbol{w}_{I,n}^H\boldsymbol{M}_n^H\boldsymbol{\Phi})\\&=\mathrm{Tr}(\boldsymbol{C}_n\boldsymbol{\Phi})\end{aligned}\tag{18}$$

where t is an auxiliary variable with unit modulus, $\boldsymbol{M}_n=[\boldsymbol{V}_n^H,\boldsymbol{h}_{D,n}]^H\in\mathbb{C}^{(L+1)\times M}$, $\bar{\boldsymbol{\phi}}=[\boldsymbol{\phi}^H,t]^H\in\mathbb{C}^{(L+1)\times 1}$, $\boldsymbol{\Phi}=\bar{\boldsymbol{\phi}}\bar{\boldsymbol{\phi}}^H\in\mathbb{C}^{(L+1)\times(L+1)}$, $\boldsymbol{C}_n=\boldsymbol{M}_n\boldsymbol{w}_{I,n}\boldsymbol{w}_{I,n}^H\boldsymbol{M}_n^H\in\mathbb{C}^{(L+1)\times(L+1)}$. Also, define $t_{I/P,n}$ ($n=-N+1,\ldots,N-1$) as

$$\begin{aligned}t_{I/P,n}&=\boldsymbol{h}^H\boldsymbol{W}_{I/P,n}\boldsymbol{h}\\&=\mathrm{Tr}(\boldsymbol{h}\boldsymbol{h}^H\boldsymbol{W}_{I/P,n})\\&=\mathrm{Tr}\left((\boldsymbol{h}_D+\boldsymbol{V}^H\boldsymbol{\phi})(\boldsymbol{h}_D^H+\boldsymbol{\phi}^H\boldsymbol{V})\boldsymbol{W}_{I/P,n}\right)\\&=\mathrm{Tr}(\boldsymbol{M}^H\boldsymbol{\Phi}\boldsymbol{M}\boldsymbol{W}_{I/P,n})\\&=\mathrm{Tr}(\boldsymbol{M}\boldsymbol{W}_{I/P,n}\boldsymbol{M}^H\boldsymbol{\Phi})\\&=\mathrm{Tr}(\boldsymbol{C}_{I/P,n}\boldsymbol{\Phi})\end{aligned}\tag{19}$$

where $\boldsymbol{V}=[\boldsymbol{V}_1,\ldots,\boldsymbol{V}_N]\in\mathbb{C}^{L\times MN}$, $\boldsymbol{M}=[\boldsymbol{V}^H,\boldsymbol{h}_D]^H\in\mathbb{C}^{(L+1)\times MN}$, $\boldsymbol{C}_{I/P,n}=\boldsymbol{M}\boldsymbol{W}_{I/P,n}\boldsymbol{M}^H\in\mathbb{C}^{(L+1)\times(L+1)}$. Therefore, the rate and objective expressions rewrite as

$$\begin{aligned}R(\boldsymbol{\Phi})&=\sum_{n=1}^{N}\log_2\left(1+\frac{(1-\rho)\mathrm{Tr}(\boldsymbol{C}_n\boldsymbol{\Phi})}{\sigma_n^2}\right),\\ z(\boldsymbol{\Phi})&=\frac{1}{2}\beta_2\rho(t_{I,0}+t_{P,0})\end{aligned}\tag{20}$$

$$z(\boldsymbol{\phi},\boldsymbol{w}_I,\boldsymbol{w}_P,\rho)=\beta_2\rho\Big(\mathcal{E}\left\{\mathcal{A}\left\{y_I^2(t)\right\}\right\}+\mathcal{A}\left\{y_P^2(t)\right\}\Big)+\beta_4\rho^2\Big(\mathcal{E}\left\{\mathcal{A}\left\{y_I^4(t)\right\}\right\}+\mathcal{A}\left\{y_P^4(t)\right\}+6\mathcal{E}\left\{\mathcal{A}\left\{y_I^2(t)\right\}\right\}\mathcal{A}\left\{y_P^2(t)\right\}\Big)\,.\tag{11}$$

$$\mathcal{E}\left\{\mathcal{A}\left\{y_I^2(t)\right\}\right\}=\frac{1}{2}\sum_{n=1}^{N}(\boldsymbol{h}_n^H\boldsymbol{w}_{I,n})(\boldsymbol{h}_n^H\boldsymbol{w}_{I,n})^H=\frac{1}{2}\boldsymbol{h}^H\boldsymbol{W}_{I,0}\boldsymbol{h}\,,\tag{12}$$

$$\mathcal{E}\left\{\mathcal{A}\left\{y_I^4(t)\right\}\right\}=\frac{3}{4}\left(\sum_{n=1}^{N}(\boldsymbol{h}_n^H\boldsymbol{w}_{I,n})(\boldsymbol{h}_n^H\boldsymbol{w}_{I,n})^H\right)^2=\frac{3}{4}(\boldsymbol{h}^H\boldsymbol{W}_{I,0}\boldsymbol{h})^2\,,\tag{13}$$

$$\mathcal{A}\left\{y_P^2(t)\right\}=\frac{1}{2}\sum_{n=1}^{N}(\boldsymbol{h}_n^H\boldsymbol{w}_{P,n})(\boldsymbol{h}_n^H\boldsymbol{w}_{P,n})^H=\frac{1}{2}\boldsymbol{h}^H\boldsymbol{W}_{P,0}\boldsymbol{h}\,,\tag{14}$$

$$\mathcal{A}\left\{y_P^4(t)\right\}=\frac{3}{8}\sum_{\substack{n_1,n_2,n_3,n_4\\ n_1+n_2=n_3+n_4}}(\boldsymbol{h}_{n_1}^H\boldsymbol{w}_{P,n_1})(\boldsymbol{h}_{n_2}^H\boldsymbol{w}_{P,n_2})(\boldsymbol{h}_{n_3}^H\boldsymbol{w}_{P,n_3})^H(\boldsymbol{h}_{n_4}^H\boldsymbol{w}_{P,n_4})^H=\frac{3}{8}\sum_{n=-N+1}^{N-1}(\boldsymbol{h}^H\boldsymbol{W}_{P,n}\boldsymbol{h})(\boldsymbol{h}^H\boldsymbol{W}_{P,n}\boldsymbol{h})^H\,.\tag{15}$$

$$+\frac{3}{8}\beta_4\rho^2\left(2t_{I,0}^2+\sum_{n=-N+1}^{N-1}t_{P,n}t_{P,n}^*\right)+\frac{3}{2}\beta_4\rho^2 t_{I,0}t_{P,0}\,. \tag{21}$$

To maximize non-concave expression 21, we propose a Successive Convex Approximation (SCA) algorithm that approximate the second-order terms by first-order Taylor expansion [37]. Based on the solution at iteration $i-1$, the approximations at iteration i are

$$(t_{I,0}^{(i)})^2 \geq 2t_{I,0}^{(i)}t_{I,0}^{(i-1)}-(t_{I,0}^{(i-1)})^2\,, \tag{22}$$

$$t_{P,n}^{(i)}(t_{P,n}^{(i)})^* \geq 2\Re\left\{t_{P,n}^{(i)}(t_{P,n}^{(i-1)})^*\right\}-t_{P,n}^{(i-1)}(t_{P,n}^{(i-1)})^*\,, \tag{23}$$

$$\begin{aligned}t_{I,0}^{(i)}t_{P,0}^{(i)} &= \frac{1}{4}(t_{I,0}^{(i)}+t_{P,0}^{(i)})^2-\frac{1}{4}(t_{I,0}^{(i)}-t_{P,0}^{(i)})^2\\ &\geq \frac{1}{2}(t_{I,0}^{(i)}+t_{P,0}^{(i)})(t_{I,0}^{(i-1)}+t_{P,0}^{(i-1)})\\ &\quad-\frac{1}{4}(t_{I,0}^{(i-1)}+t_{P,0}^{(i-1)})^2-\frac{1}{4}(t_{I,0}^{(i)}-t_{P,0}^{(i)})^2\end{aligned} \tag{24}$$

which provide lower bounds to the corresponding terms in 21. Hence, the objection function is approximated by $\tilde{z}(\boldsymbol{\Phi}^{(i)})$ in 25, and problem 17 is transformed to

$$\begin{aligned}\max_{\boldsymbol{\Phi}}\quad & \tilde{z}(\boldsymbol{\Phi}) && \text{(26a)}\\ \text{s.t.}\quad & R(\boldsymbol{\Phi})\geq\bar{R}, && \text{(26b)}\\ & \boldsymbol{\Phi}_{l,l}=1,\quad l=1,\ldots,L+1, && \text{(26c)}\\ & \boldsymbol{\Phi}\succeq 0, && \text{(26d)}\\ & \operatorname{rank}(\boldsymbol{\Phi})=1\,. && \text{(26e)}\end{aligned}$$

Problem 26 is not a standard Semidefinite Programming (SDP). If we relax the rank constraint 26e to formulate a convex problem, there is no guarantee that the optimal rank-1 solution $\bar{\boldsymbol{\phi}}^\star$ extracted from $\boldsymbol{\Phi}^\star$ is a stationary point of the original problem 17. In Section IV, we numerically show that $\boldsymbol{\Phi}^\star$ is rank-1 for all tested channel realizations and the performance loss is insignificant. A related version of problem 26 can be solved using existing optimization tools such as CVX [38].

When $\boldsymbol{\Phi}^\star$ is rank-1, the optimal phase shift vector $\bar{\boldsymbol{\phi}}^\star$ can be obtained by Eigenvalue Decomposition (EVD). Otherwise, a suboptimal solution can be extracted via Gaussian randomization method [39]. Specifically, we perform EVD $\boldsymbol{\Phi}^\star=\boldsymbol{U}\boldsymbol{\Sigma}\boldsymbol{U}^H$, generate Q CSCG random vectors $\boldsymbol{r}_q\sim\mathcal{CN}(\boldsymbol{0},\boldsymbol{I}_{L+1}),\ q=1,\ldots,Q$, construct the corresponding candidates $\bar{\boldsymbol{\phi}}_q=e^{j\arg\left(\boldsymbol{U}\boldsymbol{\Sigma}^{1/2}\boldsymbol{r}_q\right)}$, and choose the one that maximizes the objective function 26a. Finally, the phase shift is retrieved by $\theta_l=\arg(\phi_l^\star/\phi_{L+1}^\star),\ l=1,\ldots,L$. The SCA algorithm for IRS phase shift optimization is summarized in Algorithm 1.

Algorithm 1 SCA: IRS Phase Shift.

input $\beta_2,\beta_4,\boldsymbol{h}_{D,n},\boldsymbol{H}_{I,n},\boldsymbol{h}_{R,n},\boldsymbol{w}_I,\boldsymbol{w}_P,\rho,\sigma_n,\bar{R},Q,\epsilon$
Construct $\boldsymbol{M},\boldsymbol{M}_n,\boldsymbol{C}_n$ for $n=1,\ldots,N$, $\boldsymbol{C}_{I/P,n}$ for $n=-N+1,\ldots,N-1$
initialize $i\leftarrow 0,\boldsymbol{\Phi}^{(0)},t_{I/P,n}^{(0)}$ for $n=-N+1,\ldots,N-1$
repeat
  $i\leftarrow i+1$
  Obtain $\boldsymbol{\Phi}^{(i)},t_{I/P,n}^{(i)}$ by solving problem 26
  Compute $z^{(i)}$ by 21
until $|z^{(i)}-z^{(i-1)}|\leq\epsilon$
Set $\boldsymbol{\Phi}^\star=\boldsymbol{\Phi}^{(i)}$
if $\operatorname{rank}(\boldsymbol{\Phi}^\star)=1$ **then**
  Obtain $\bar{\boldsymbol{\phi}}^\star$ by EVD, $\boldsymbol{\Phi}^\star=\bar{\boldsymbol{\phi}}^\star(\bar{\boldsymbol{\phi}}^\star)^H$
else
  Obtain $\boldsymbol{U},\boldsymbol{\Sigma}$ by EVD, $\boldsymbol{\Phi}^\star=\boldsymbol{U}\boldsymbol{\Sigma}\boldsymbol{U}^H$
  Generate $\boldsymbol{r}_q\sim\mathcal{CN}(\boldsymbol{0},\boldsymbol{I}_{L+1}),\ q=1,\ldots,Q$
  Construct $\bar{\boldsymbol{\phi}}_q=e^{j\arg\left(\boldsymbol{U}\boldsymbol{\Sigma}^{1/2}\boldsymbol{r}_q\right)},\ \boldsymbol{\Phi}_q=\bar{\boldsymbol{\phi}}_q\bar{\boldsymbol{\phi}}_q^H$
  Set $q^\star=\arg\max_q z(\boldsymbol{\Phi}_q),\ \bar{\boldsymbol{\phi}}^\star=\bar{\boldsymbol{\phi}}_{q^\star}$
end if
Set $\theta_l^\star=\arg(\phi_l^\star/\phi_{L+1}^\star),\ l=1,\ldots,L$, construct $\boldsymbol{\phi}^\star$
output $\boldsymbol{\phi}^\star$

B. Waveform and Splitting Ratio

Next, we jointly optimize both information and power waveforms $\boldsymbol{w}_{I/P}$ together with splitting ratio ρ for any given IRS phase shift $\boldsymbol{\phi}$. As pointed out in [12], the waveform design in frequency and spatial domain can be decoupled without performance loss, and the optimal spatial weight is given by Maximum-Ratio Transmission (MRT) beamformer

$$\boldsymbol{w}_{I/P,n}=s_{I/P,n}\frac{\boldsymbol{h}_n}{\|\boldsymbol{h}_n\|}\,. \tag{27}$$

That is to say, for single-user MISO SWIPT, it is only necessary to determine the amplitudes $s_{I/P,n}$ at different tones. Hence, the original waveform optimization with $2MN$ complex variables is converted into a power allocation problem with $2N$ nonnegative real variables. Let $\boldsymbol{s}_{I/P}=[s_{I/P,1},\ldots,s_{I/P,N}]^T\in\mathbb{C}^{N\times 1}$. At subband n, the effective channel gain is given by $\|\boldsymbol{h}_n\|$, and the power allocated to the modulated and unmodulated waveform are given by $s_{I,n}^2$ and $s_{P,n}^2$, respectively. With such an active beamformer selection, we have $\boldsymbol{h}_n^H\boldsymbol{w}_{I,n}=|\boldsymbol{h}_n^H\boldsymbol{w}_{I,n}|=$

$$\begin{aligned}\tilde{z}(\boldsymbol{\Phi}^{(i)}) &= \frac{1}{2}\beta_2\rho(t_{I,0}^{(i)}+t_{P,0}^{(i)})\\ &\quad+\frac{3}{8}\beta_4\rho^2\left(4(t_{I,0}^{(i)})(t_{I,0}^{(i-1)})-2(t_{I,0}^{(i-1)})^2+\sum_{n=-N+1}^{N-1}2\Re\left\{t_{P,n}^{(i)}(t_{P,n}^{(i-1)})^*\right\}-t_{P,n}^{(i-1)}(t_{P,n}^{(i-1)})^*\right)\\ &\quad+\frac{3}{2}\beta_4\rho^2\left(\frac{1}{2}(t_{I,0}^{(i)}+t_{P,0}^{(i)})(t_{I,0}^{(i-1)}+t_{P,0}^{(i-1)})-\frac{1}{4}(t_{I,0}^{(i-1)}+t_{P,0}^{(i-1)})^2-\frac{1}{4}(t_{I,0}^{(i)}-t_{P,0}^{(i)})^2\right)\,.\end{aligned} \tag{25}$$

$\|\boldsymbol{h}_n\|s_{I,n}$ such that the rate and objective function further reduces to 28 and 29, respectively.

$$R(\boldsymbol{s}_I,\rho)=\log_2\left(\prod_{n=1}^{N}\left(1+\frac{(1-\rho)\|\boldsymbol{h}_n\|^2 s_{I,n}^2}{\sigma_n^2}\right)\right). \quad (28)$$

Therefore, problem 17 is reduced to an amplitude optimization issue

$$\max_{\boldsymbol{s}_I,\boldsymbol{s}_P,\rho} \quad z(\boldsymbol{s}_I,\boldsymbol{s}_P,\rho) \quad (30a)$$
$$\text{s.t.} \quad \frac{1}{2}\left(\|\boldsymbol{s}_I\|^2+\|\boldsymbol{s}_P\|^2\right)\le P, \quad (30b)$$
$$R(\boldsymbol{s}_I,\rho)\ge \bar{R}\,. \quad (30c)$$

Since problem 30 involves the production of nonnegative real variables, we introduce auxiliary variables $t',\bar{\rho}$ and transform it into a reversed GP

$$\min_{\boldsymbol{s}_I,\boldsymbol{s}_P,\rho,\bar{\rho},t'} \quad \frac{1}{t'} \quad (31a)$$
$$\text{s.t.} \quad \frac{1}{2}\left(\|\boldsymbol{s}_I\|^2+\|\boldsymbol{s}_P\|^2\right)\le P, \quad (31b)$$
$$\frac{t'}{z(\boldsymbol{s}_I,\boldsymbol{s}_P,\rho)}\le 1, \quad (31c)$$
$$\frac{2^{\bar{R}}}{\prod_{n=1}^{N}\left(1+\bar{\rho}\|\boldsymbol{h}_n\|^2 s_{I,n}^2/\sigma_n^2\right)}\le 1, \quad (31d)$$
$$\rho+\bar{\rho}\le 1\,. \quad (31e)$$

The denominators of 31c, 31d are posynomials [40], which is further decomposed as

$$z(\boldsymbol{s}_I,\boldsymbol{s}_P,\rho)=\sum_{m_P} g_{m_P}(\boldsymbol{s}_I,\boldsymbol{s}_P,\rho)\,, \quad (32)$$
$$1+\frac{\bar{\rho}\|\boldsymbol{h}_n\|^2 s_{I,n}^2}{\sigma_n^2}=\sum_{m_{I,n}} g_{m_{I,n}}(s_{I,n},\bar{\rho}) \quad (33)$$

where $m_P, m_{I,n}$ are the number of monomials in the corresponding posynomials (obviously $m_{I,n}=2$). Following [41], we upper bound posynomials 32 and 33 by Arithmetic Mean-Geometric Mean (AM-GM) inequality such that problem 31 reduces to

$$\min_{\boldsymbol{s}_I,\boldsymbol{s}_P,\rho,\bar{\rho},t'} \quad \frac{1}{t'} \quad (34a)$$
$$\text{s.t.} \quad \frac{1}{2}\left(\|\boldsymbol{s}_I\|^2+\|\boldsymbol{s}_P\|^2\right)\le P, \quad (34b)$$
$$t'\prod_{m_P}\left(\frac{g_{m_P}(\boldsymbol{s}_I,\boldsymbol{s}_P,\rho)}{\gamma_{m_P}}\right)^{-\gamma_{m_P}}\le 1, \quad (34c)$$
$$2^{\bar{R}}\prod_{n}\prod_{m_{I,n}}\left(\frac{g_{m_{I,n}}(s_{I,n},\bar{\rho})}{\gamma_{m_{I,n}}}\right)^{-\gamma_{m_{I,n}}}\le 1, \quad (34d)$$
$$\rho+\bar{\rho}\le 1 \quad (34e)$$

where $\gamma_{m_P},\gamma_{m_{I,n}}\ge 0$, $\sum_{m_P}\gamma_{m_P}=\sum_{m_{I,n}}\gamma_{m_{I,n}}=1$. The tightness of the AM-GM inequality depends on $\{\gamma_{m_P},\gamma_{m_{I,n}}\}$ that require successive update. As suggested in [12], a feasible choice at iteration i is

$$\gamma_{m_P}^{(i)}=\frac{g_{m_P}(\boldsymbol{s}_I^{(i-1)},\boldsymbol{s}_P^{(i-1)},\rho^{(i-1)})}{z(\boldsymbol{s}_I^{(i-1)},\boldsymbol{s}_P^{(i-1)},\rho^{(i-1)})}\,, \quad (35)$$
$$\gamma_{m_{I,n}}^{(i)}=\frac{g_{m_{I,n}}(s_{I,n}^{(i-1)},\bar{\rho}^{(i-1)})}{1+\bar{\rho}^{(i-1)}\|\boldsymbol{h}_n\|^2(s_{I,n}^{(i-1)})^2/\sigma_n^2}\,. \quad (36)$$

Problem 34 can be solved using existing optimization tools such as CVX [38]. $\boldsymbol{s}_I,\boldsymbol{s}_P,\rho$ are updated iteratively until convergence. The GP algorithm of waveform and splitting ratio optimization is summarized in Algorithm 2.

Algorithm 2 GP: Waveform and Splitting Ratio.

input $\beta_2,\beta_4,\boldsymbol{h},P,\sigma_n,\bar{R},\epsilon$
initialize $i\leftarrow 0$, $\boldsymbol{s}_{I/P}^{(0)}$, $\rho^{(0)}$
repeat
  $i\leftarrow i+1$
  Update $\{\gamma_{m_P}^{(i)},\gamma_{m_{I,n}}^{(i)}\}$ by 35, 36
  Obtain $\boldsymbol{s}_{I/P}^{(i)},\rho^{(i)}$ by solving problem 34
  Compute $z^{(i)}$ by 29
until $|z^{(i)}-z^{(i-1)}|\le\epsilon$
Set $\boldsymbol{s}_{I/P}^{\star}=\boldsymbol{s}_{I/P}^{(i)}$, $\rho^{\star}=\rho^{(i)}$, retrieve $\boldsymbol{w}_{I/P}^{\star}$ by 27
output $\boldsymbol{w}_{I/P}^{\star},\rho^{\star}$

$$\begin{aligned} z(\boldsymbol{s}_I,\boldsymbol{s}_P,\rho)=&\frac{1}{2}\beta_2\rho\sum_{n=1}^{N}\|\boldsymbol{h}_n\|^2(s_{I,n}^2+s_{P,n}^2)\\ &+\frac{3}{8}\beta_4\rho^2\left(2\sum_{n_1,n_2}\prod_{j=1}^{2}\|\boldsymbol{h}_{n_j}\|^2 s_{I,n_j}^2+\sum_{\substack{n_1,n_2,n_3,n_4\\ n_1+n_2=n_3+n_4}}\prod_{j=1}^{4}\|\boldsymbol{h}_{n_j}\|s_{P,n_j}\right)\\ &+\frac{3}{2}\beta_4\rho^2\left(\sum_{n_1,n_2}\|\boldsymbol{h}_{n_1}\|^2 s_{I,n_1}^2\|\boldsymbol{h}_{n_2}\|^2 s_{P,n_2}^2\right). \end{aligned} \quad (29)$$

Algorithm 3 AO: Waveform, Active and Passive Beamforming.

1: **input** $\beta_2, \beta_4, \boldsymbol{h}_{D,n}, \boldsymbol{H}_{I,n}, \boldsymbol{h}_{R,n}, P, \sigma_n, \bar{R}, Q, \epsilon$
2: **initialize** $i \leftarrow 0$, $\boldsymbol{\phi}^{(0)}, \boldsymbol{w}_{I/P}^{(0)}, \rho^{(0)}$
3: **repeat**
4: $i \leftarrow i+1$
5: Fix $\boldsymbol{w}_{I/P}^{(i-1)}, \rho^{(i-1)}$ and obtain $\boldsymbol{\phi}^{(i)}$ by Algorithm 1
6: Fix $\boldsymbol{\phi}^{(i)}$, update $\boldsymbol{h}_n^{(i)}$ by 4, and obtain $\boldsymbol{w}_{I/P}^{(i)}, \rho^{(i)}$ by Algorithm 2
7: Compute $z^{(i)}$ by 21
8: **until** $|z^{(i)} - z^{(i-1)}| \leq \epsilon$
9: **output** $\boldsymbol{\phi}^\star, \boldsymbol{w}_{I/P}^\star, \rho^\star$

C. Alternating Optimization

For any direct, incident and reflective channels, we iteratively update the passive beamforming by Algorithm 1 and waveform, active beamforming, splitting ratio by Algorithm 2 until convergence. The AO algorithm is summarized in Algorithm 3.

D. Convergence

Proposition 1. *For any feasible initial point, the proposed SCA-based Algorithm 1 can provide a feasible $\boldsymbol{\Phi}^\star$ that satisfy the KKT conditions, although there is no guarantee $\boldsymbol{\Phi}^\star$ is rank-*1*. (Numerical results proved that $\boldsymbol{\Phi}^\star$ is rank-*1* for all tested channel realizations under different configurations.)*

Proof. The objective function 26a is non-decreasing over iterations because the solution of problem 26 at iteration $i-1$ is still a feasible point at iteration i. Moreover, the sequence $\{\tilde{z}(\boldsymbol{\Phi}^{(i)})\}_{i=1}^{\infty}$ is bounded above due to the unit-modulus constraint 26c. Thus, Algorithm 1 is guaranteed to converge. To prove $\boldsymbol{\Phi}^{(i)}$ converge to the set of stationary points of IRS subproblem, we notice that the SCA-based Algorithm 1 is indeed an inner approximation algorithm [42], since $\tilde{z}(\boldsymbol{\Phi}) \leq z(\boldsymbol{\Phi})$, $\partial\tilde{z}(\boldsymbol{\Phi}^{(i)})/\partial\boldsymbol{\Phi} = \partial z(\boldsymbol{\Phi}^{(i)})/\partial\boldsymbol{\Phi}$ and the approximation 22 – 24 are asymptotically tight as $i \to \infty$ [37], [43]. Therefore, Algorithm 1 is guaranteed to provide a feasible $\boldsymbol{\Phi}^\star$ that satisfy the KKT conditions. □

Proposition 2. *For any feasible initial point, the GP-based Algorithm 2 is guaranteed to converge to a stationary point of the waveform and splitting ratio subproblem.*

Proof. See [8], [12]. □

Proposition 3. *Every limit point $(\boldsymbol{\phi}^\star, \boldsymbol{w}_I^\star, \boldsymbol{w}_P^\star, \rho^\star)$ of the proposed alternating algorithm is a stationary point of the original problem 17.*

Proof. The objective function 17a is non-decreasing over iterations of Algorithm 3, which is also upper-bounded due to the unit-modulus constraint 17d and the average transmit power constraint 17b. Thus, Algorithm 3 is guaranteed to converge, namely the sequence $\{\boldsymbol{\phi}^{(i)}, \boldsymbol{w}_I^{(i)}, \boldsymbol{w}_P^{(i)}, \rho^{(i)}\}$ generated by optimizing $\boldsymbol{\phi}$ and $\boldsymbol{w}_I, \boldsymbol{w}_P, \rho$ alternatively has limit points. As demonstrated in [44]–[46], the solution is a stationary point of problem 17. □

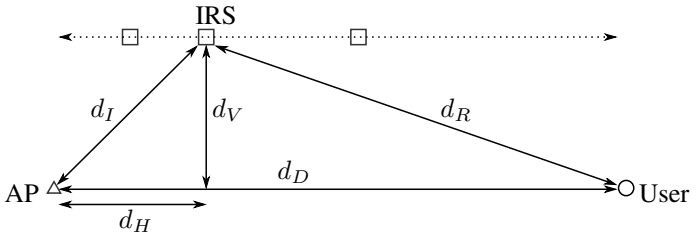

Fig. 3. System layout in the simulation.

IV. Performance Evaluations

To evaluate the performance of the proposed IRS-aided SWIPT system, we characterize the average R-E regions under typical setups. Consider a large open space WiFi-like environment at a center frequency of $5.18\,\mathrm{GHz}$ with reference bandwidth $B = 1\,\mathrm{MHz}$. As shown in Fig. 3, we assume the IRS moves along a horizontal line parallel to the AP-user path and let d_H, d_V be the horizontal and vertical distances from the AP to the IRS, respectively. We also denote d_D, d_I, d_R as the length of direct, incident, reflective paths such that $d_I = \sqrt{d_H^2 + d_V^2}$, $d_R = \sqrt{(d_D - d_H)^2 + d_V^2}$. Choose $d_D = 15\,\mathrm{m}$, $d_V = 2\,\mathrm{m}$ and reference $d_H = 2\,\mathrm{m}$. The path loss and fading parameters are obtained from IEEE TGn channel model D [47], and reference path loss is set to $L_0 = -35\,\mathrm{dB}$ at $d_0 = 1\,\mathrm{m}$. We assume all channels are NLoS with taps modelled as i.i.d. CSCG random variables of unit average sum-power to create a normalized multipath response. The reference numbers of transmit antennas, IRS reflectors and subbands are $M = 1$, $L = 20$, $N = 16$, respectively. No spatial correlation is considered across transmit antenna and IRS arrays. Rectenna parameters are taken as $k_2 = 0.0034$, $k_4 = 0.3829$, $R_{\text{ant}} = 50\,\Omega$. With $0\,\mathrm{dBi}$ transmit antenna gain, the average Effective Isotropic Radiated Power (EIRP) is fixed to $P = -36\,\mathrm{dBm}$ while the reference average noise power is $\sigma_n = -40\,\mathrm{dBm}$ at all subbands. We also assume $0\,\mathrm{dBi}$ IRS element gain and $2\,\mathrm{dBi}$ receive antenna gain. For the algorithm, the tolerance is $\epsilon = 10^{-8}$, the number of candidates in the Gaussian randomization method is $Q = 10^3$, and the R-E region is averaged over 200 channel realizations. In the R-E boundary, the leftmost point corresponds to WPT ($\rho = 1$) where power can be allocated simultaneously to modulated and unmodulated waveform to maximize the average output DC current. On the other hand, the rightmost point corresponds to WIT ($\rho = 0$) where the solution coincides with the Water-Filling (WF) algorithm that allocates all power to modulated waveform only. For a fair comparison, the x-axis of the plots has been normalized to per-subband rate.

We first evaluate the performance of Algorithm 1 under SDR. It is demonstrated that $\boldsymbol{\Phi}^\star$ is rank-1 for all tested channel realizations with different M, N and L. Therefore, $\boldsymbol{\phi}^\star$ can be directly obtained through EVD and we claim Algorithm 1 converges to stationary points of problem 26 without performance loss.

Fig. 4 illustrates the average R-E region versus the number of subband N. *First*, it is observed that increasing N reduces the per-subband rate but boosts the harvested energy. The reason is that although each subband receives a smaller proportion

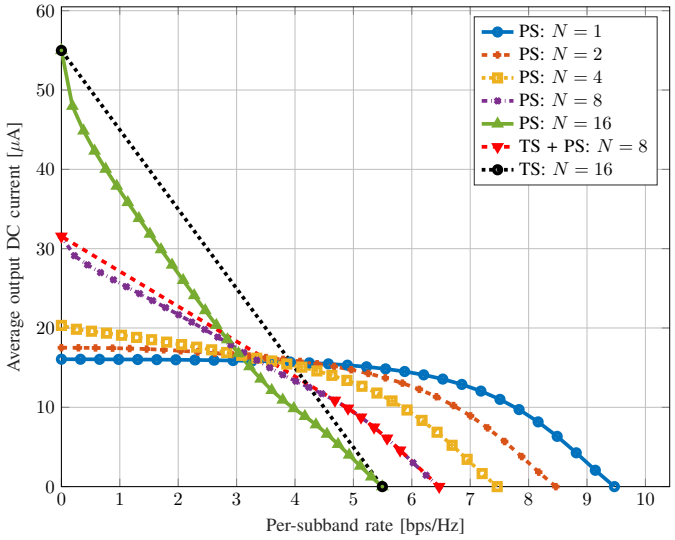

Fig. 4. Average R-E region versus N for $M = 1$, $L = 20$, $\sigma_n = -40\,\text{dBm}$, $B = 1\,\text{MHz}$ and $d_H = 2\,\text{m}$.

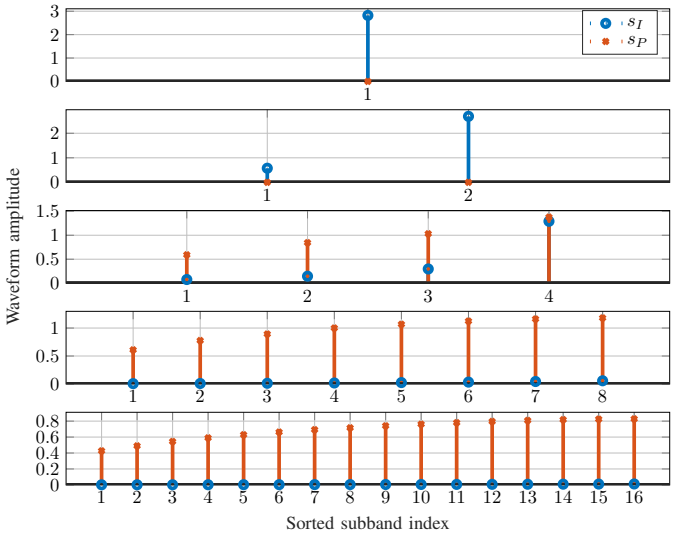

Fig. 5. WPT-optimized waveform amplitudes versus N for $M = 1$, $L = 20$, $\sigma_n = -40\,\text{dBm}$, $B = 1\,\text{MHz}$ and $d_H = 2\,\text{m}$.

of the total power, more balanced terms are introduced to further amplify the output DC current, as suggested by the scaling laws in [12]. Sorted waveform amplitudes in Fig. 5 also confirmed that from the perspective of WPT, dedicated multisine waveform is unnecessary for a small N but is required for a large N. As shown in 13 and 15, the only difference of modulated and unmodulated waveform on z exists in the fourth-order terms, where $\mathcal{E}\left\{\mathcal{A}\left\{y_I^4(t)\right\}\right\}$ has N^2 monomials with a modulation gain of 2 and $\mathcal{A}\left\{y_P^4(t)\right\}$ has $(2N^3+N)/3$ monomials without modulation gain. Therefore, superposed waveform enlarges the R-E region for a sufficiently large N (typically no smaller than 4). However, an excessively large N not only increases complexity but also operates out of the small-signal harvester model, thus become prohibitive. *Second*, the R-E region is convex for $N = 2, 4$ and concave-convex for $N = 8, 16$. This has the consequence that PS outperforms TS

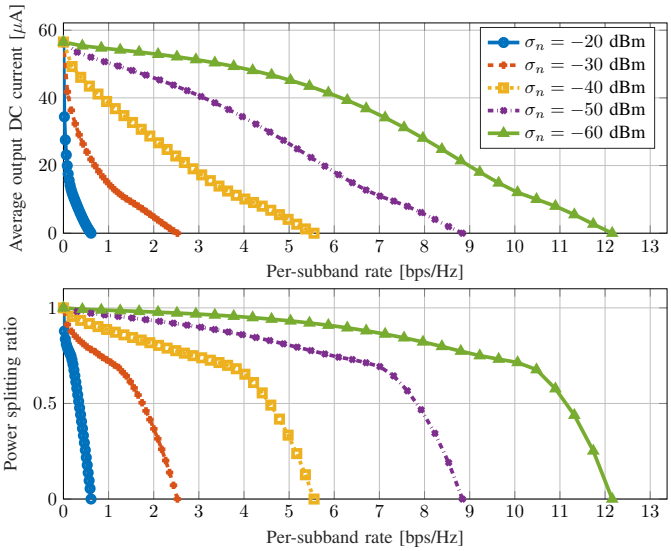

Fig. 6. Average R-E region and splitting ratio versus σ_n for $M = 1$, $N = 16$, $L = 20$, $B = 1\,\text{MHz}$ and $d_H = 2\,\text{m}$.

for a small N and is outperformed for a large N. When N is in between, the optimal strategy is a combination of both, i.e. a time sharing between the WPT point and the tangent WIPT point obtained by PS. Compared with the linear harvester model that requires no dedicated power waveform and always prefer PS, the rectifier nonlinearity enlarges the R-E region by favouring a different waveform and transceiving strategy, both heavily depends on N.

The influence of the average noise power on the average R-E region is investigated in Fig. 6. We *first* note that for a large number of subbands, the R-E region is approximately concave for a high noise level and approximately convex for a low noise level. Hence, TS is preferred at low SNR while PS is preferred at high SNR. This is because at a low SNR, the capacity-achieving WF algorithm tends to allocate more power to few strongest subbands. As the rate constraint $\bar{R}$ decreases, more subbands are activated to further boost the harvested energy via the coupling effect by rectifier nonlinearity. *Second*, there exists a turning point in the R-E region especially for a small noise ($\sigma_n \leq -40\,\text{dBm}$). The reason is that when $\bar{R}$ departs slightly from the maximum achievable rate, the algorithm mainly adjusts the splitting ratio ρ rather than put more weight on the multisine waveform, as a small amplitude could be inefficient for energy maximization. On the other hand, as $\bar{R}$ further reduces, a modulated waveform with a very large ρ could be outperformed by a superposed waveform with a smaller ρ, due to advantage the of multisine. The result highlights the necessity of joint optimization of waveform and splitting ratio.

In Fig. 7, we compare the average R-E region achieved by different AP-IRS horizontal distance d_H. A *first* observation is that, different from the active relay that favors the midpoint development, placing the IRS closer to either the AP or the user would further improve the R-E tradeoff. It origins from the product-distance path loss model that applies to finite-size element reflection. As shown in Fig. 8, although the piecewise

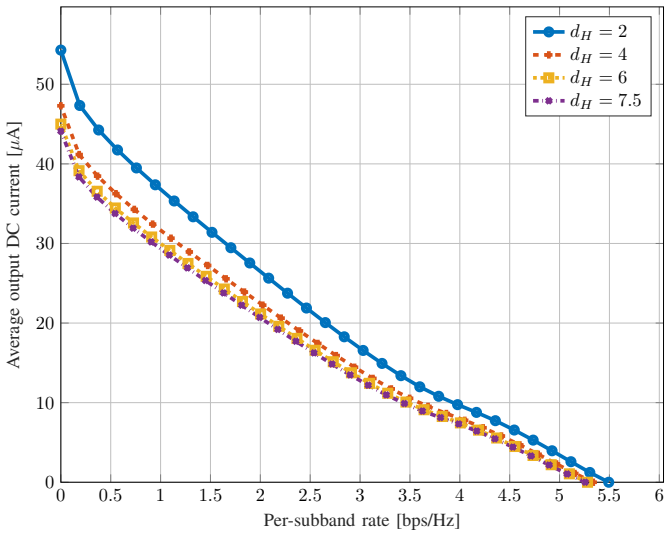

Fig. 7. Average R-E region versus d_H for $M = 1$, $N = 16$, $L = 20$, $\sigma_n = -40\,\text{dBm}$ and $B = 1\,\text{MHz}$.

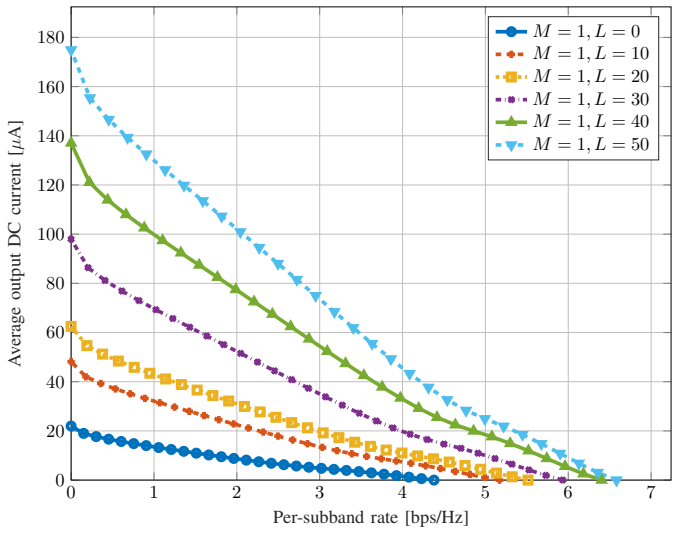

Fig. 9. Average R-E region versus L for $M = 1$, $N = 16$, $\sigma_n = -40\,\text{dBm}$, $B = 1\,\text{MHz}$ and $d_H = 2\,\text{m}$.

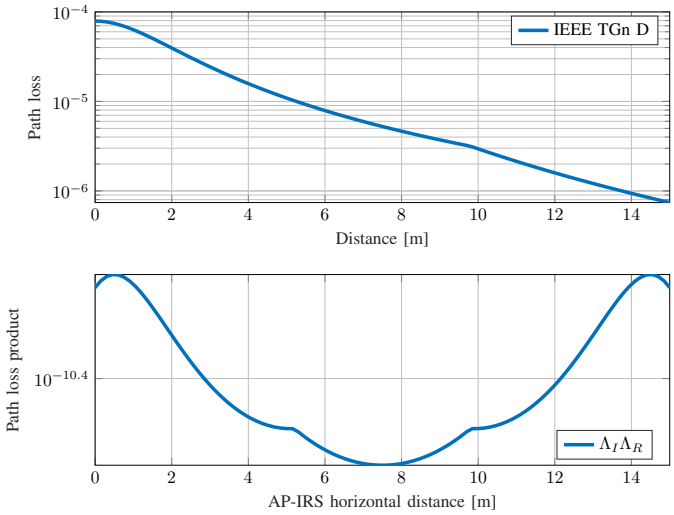

Fig. 8. Path loss versus distance for IEEE TGn channel model D.

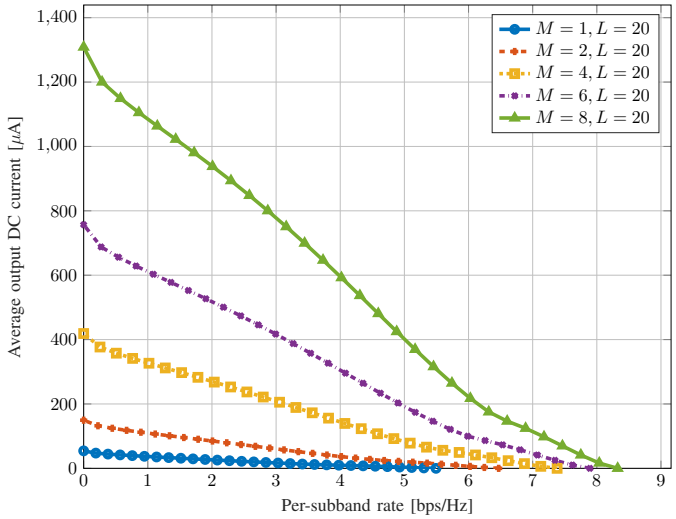

Fig. 10. Average R-E region versus M for $N = 16$, $L = 20$, $\sigma_n = -40\,\text{dBm}$, $B = 1\,\text{MHz}$ and $d_H = 2\,\text{m}$.

TGn path loss model further penalizes large distance (greater than $10\,\text{m}$ for model D), it is still beneficial to have a short-long or long-short transmission setup, since signal attenuation increases fast at a short distance and experiences marginal effect at a long distance. On the other hand, it also suggests that developing an IRS next to the AP can effectively extend the operation range of SWIPT systems. Considering the passive characteristic of IRS, opportunities are that it can be directly supported by the SWIPT network. A *second* observation is that there exist two optimal IRS development locations that maximizes the path loss production $\Lambda_I\Lambda_R$. It implies that more than one IRS may be implemented to further enlarge the R-E region, one attached to the AP and one attached to the IRS.

The impact of the number of transmit antennas M and IRS reflectors L on the average R-E tradeoff is revealed in Fig. 9 and 10. A *first* contrast indicates that adding either active or passive elements benefits both information and power transmission while preserving the concavity-convexity of the R-E region. This is because increasing M or L indeed enhances the equivalent composite channel strength such that the magnitude of the components in 11 is amplified while the number of components remains unchanged. Therefore, we conclude that the number of transmit antennas and reflectors have no impact on the waveform preference and transceiving strategy. A *second* contrast suggests that active beamforming is more effective than passive beamforming, as the system performance is more sensitive to the variation of M than L. Interestingly, the active MRT beamformer only has a transmit array gain of M. In comparison, the IRS collects L signal copies with a receive array gain L, then performs an equal gain reflection with a reflect array gain L, achieving a total array gain of L^2. However, the system performance in our setup is dominated by the direct link. As shown in Fig. 8, the direct path loss Λ_D is in the scope of 10^{-7} while the extra path loss product $\Lambda_I\Lambda_R$ is below 10^{-10}. Therefore, despite increasing L can effectively enhance

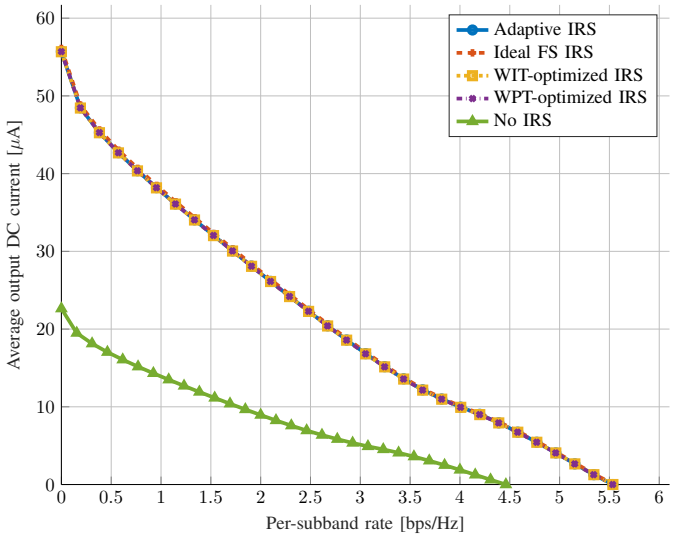

Fig. 11. Average R-E region for adaptive, ideal, fixed and no IRS over $B = 1\,\text{MHz}$ for $M = 1$, $N = 16$, $L = 20$, $\sigma_n = -40\,\text{dBm}$ and $d_H = 2\,\text{m}$.

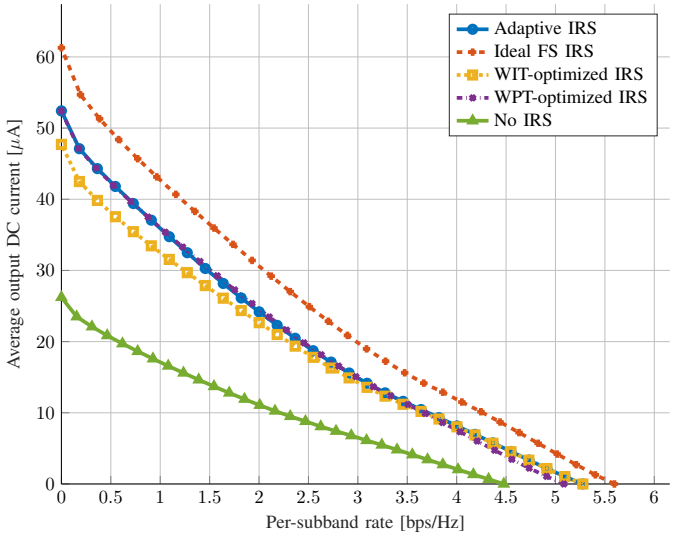

Fig. 12. Average R-E region for adaptive, ideal, fixed and no IRS over $B = 10\,\text{MHz}$ for $M = 1$, $N = 16$, $L = 20$, $\sigma_n = -40\,\text{dBm}$ and $d_H = 2\,\text{m}$.

the AP-IRS-user extra channel, its amplitude is still too small compared with the AP-user channel such that increasing M is more effective to improve the system performance.

Fig. 11 and 12 explore the average R-E region under different IRS configuration for narrowband transmission and broadband transmission. The adaptive scheme optimizes the IRS and waveform alternatively for each points in the R-E boundary. In comparison, the WIT/WPT-based schemes only perform alternating optimization for the right-most/left-most points, then fix the IRS and update the waveform to obtain the R-E curve. To gain some insight into the IRS behavior, we compare the results above to that of no IRS and the ideal FS IRS, where we assume each element has an independent reflection coefficient for each subband such that the ideal IRS has a total design flexibility of NL. Since the IRS only control the phase of the concatenated channel, the optimal strategy for each FS reflector in the presence of single transmit antenna would be aligning the AP-IRS-user and AP-user channel over all subbands, namely

$$\theta_{l,n}^{\star} = e^{j \arg\left(h_{D,n}/(h_{I,n,l} h_{R,n,l})\right)}, \quad \forall n, l\,. \tag{37}$$

First, it is observed that the presence of IRS effectively enlarges the achievable R-E region in both cases. This is because IRS creates and adapts the weak extra channels such that they add constructively to enhance the composite channel. *Second*, the performance gaps of the adaptive, ideal and fixed IRS are negligible for narrowband transmission but noticeable for broadband transmission. The reason is that when $B = 1\,\text{MHz}$, all channels are approximately flat and the response of all subbands are roughly the same. In such cases, the additional design flexibility provided by the frequency selectivity of the ideal IRS would be unnecessary, because the the optimal reflection coefficients would almost align at all subbands. Similarly, WIT-optimized and WPT-optimized IRS boil down to optimizing a single term that represents the composite channel response at all subbands. As a consequence, all IRS strategies coincide with each other, and the optimal IRS for single transmit antenna narrowband SWIPT can be approximated by any candidate that roughly align the AP-IRS-user channel with the AP-user channel simultaneously over all subbands. On the other hand, the channel frequency selectivity becomes significant for $B = 10\,\text{MHz}$, and the ideal FS IRS outperforms the others as it requires no tradeoff in subchannel alignments. Moreover, the WIT-optimized IRS tends to equalize the channel strength for all subbands as possible, due to the preference of WF strategy at high SNR. In comparison, the WPT-optimized IRS beams less towards few weakest subchannels, due to the inefficiency of small-amplitude tones in energy harvesting. Therefore, the adaptive IRS design is more suitable for broadband SWIPT. Note that the tradeoff for practical IRS indeed origins from frequency selectivity rather than number of subbands.

REFERENCES

[1] B. Clerckx, R. Zhang, R. Schober, D. W. K. Ng, D. I. Kim, and H. V. Poor, "Fundamentals of wireless information and power transfer: From RF energy harvester models to signal and system designs," *IEEE Journal on Selected Areas in Communications*, vol. 37, no. 1, pp. 4–33, 2019.

[2] L. R. Varshney, "Transporting information and energy simultaneously," *IEEE International Symposium on Information Theory - Proceedings*, pp. 1612–1616, 2008.

[3] X. Zhou, R. Zhang, and C. K. Ho, "Wireless information and power transfer: Architecture design and rate-energy tradeoff," *IEEE Transactions on Communications*, vol. 61, no. 11, pp. 4754–4767, 2013.

[4] R. Zhang and C. K. Ho, "MIMO broadcasting for simultaneous wireless information and power transfer," *IEEE Transactions on Wireless Communications*, vol. 12, no. 5, pp. 1989–2001, 2013.

[5] J. Park and B. Clerckx, "Joint wireless information and energy transfer in a K-user MIMO interference channel," *IEEE Transactions on Wireless Communications*, vol. 13, no. 10, pp. 5781–5796, 2014.

[6] M. S. Trotter, J. D. Griffin, and G. D. Durgin, "Power-optimized waveforms for improving the range and reliability of RFID systems," *2009 IEEE International Conference on RFID, RFID 2009*, pp. 80–87, 2009.

[7] B. Clerckx and J. Kim, "On the Beneficial Roles of Fading and Transmit Diversity in Wireless Power Transfer with Nonlinear Energy Harvesting," *IEEE Transactions on Wireless Communications*, vol. 17, no. 11, pp. 7731–7743, 2018.

[8] B. Clerckx and E. Bayguzina, "Waveform Design for Wireless Power Transfer," *IEEE Transactions on Signal Processing*, vol. 64, no. 23, pp. 6313–6328, 2016.

[9] J. Kim, B. Clerckx, and P. D. Mitcheson, "Experimental Analysis of Harvested Energy and Throughput Trade-off in a Realistic SWIPT System," 2019. [Online]. Available: http://arxiv.org/abs/1908.08272

[10] ——, "Signal and System Design for Wireless Power Transfer : Prototype, Experiment and Validation," pp. 1–31, 2019. [Online]. Available: http://arxiv.org/abs/1901.01156

[11] J. Kim and B. Clerckx, "Range Expansion for Wireless Power Transfer: A Joint Beamforming and Waveform Architecture," pp. 1–6, 2020. [Online]. Available: http://arxiv.org/abs/2010.01680

[12] B. Clerckx, "Wireless Information and Power Transfer: Nonlinearity, Waveform Design, and Rate-Energy Tradeoff," *IEEE Transactions on Signal Processing*, vol. 66, no. 4, pp. 847–862, 2018.

[13] M. Varasteh, B. Rassouli, and B. Clerckx, "On Capacity-Achieving Distributions for Complex AWGN Channels Under Nonlinear Power Constraints and their Applications to SWIPT," vol. 2017, 2017. [Online]. Available: http://arxiv.org/abs/1712.01226

[14] ——, "SWIPT Signaling over Frequency-Selective Channels with a Nonlinear Energy Harvester: Non-Zero Mean and Asymmetric Inputs," *IEEE Transactions on Communications*, vol. 67, no. 10, pp. 7195–7210, 2019.

[15] M. Varasteh, J. Hoydis, and B. Clerckx, "Learning to Communicate and Energize: Modulation, Coding and Multiple Access Designs for Wireless Information-Power Transmission," pp. 1–30, 2019. [Online]. Available: http://arxiv.org/abs/1909.06492

[16] D. H. Kim and J. I. Choi, "Design of a multiband frequency selective surface," *ETRI Journal*, vol. 28, no. 4, pp. 506–508, 2006.

[17] R. S. Anwar, L. Mao, and H. Ning, "Frequency selective surfaces: A review," *Applied Sciences (Switzerland)*, vol. 8, no. 9, pp. 1–47, 2018.

[18] T. J. Cui, M. Q. Qi, X. Wan, J. Zhao, and Q. Cheng, "Coding metamaterials, digital metamaterials and programmable metamaterials," *Light: Science & Applications*, vol. 3, no. 10, pp. e218–e218, 2014.

[19] C. Liaskos, S. Nie, A. Tsioliaridou, A. Pitsillides, S. Ioannidis, and I. Akyildiz, "Realizing Wireless Communication Through Software-Defined HyperSurface Environments," *19th IEEE International Symposium on a World of Wireless, Mobile and Multimedia Networks, WoWMoM 2018*, 2018.

[20] Q. Wu and R. Zhang, "Intelligent Reflecting Surface Enhanced Wireless Network: Joint Active and Passive Beamforming Design," in *2018 IEEE Global Communications Conference (GLOBECOM)*, vol. 18, no. 11. IEEE, dec 2018, pp. 1–6. [Online]. Available: http://arxiv.org/abs/1809.01423https://ieeexplore.ieee.org/document/8647620/

[21] ——, "Beamforming Optimization for Intelligent Reflecting Surface with Discrete Phase Shifts," in *ICASSP 2019 - 2019 IEEE International Conference on Acoustics, Speech and Signal Processing (ICASSP)*. IEEE, may 2019, pp. 7830–7833. [Online]. Available: https://ieeexplore.ieee.org/document/8683145/

[22] ——, "Intelligent Reflecting Surface Enhanced Wireless Network via Joint Active and Passive Beamforming," *IEEE Transactions on Wireless Communications*, vol. 18, no. 11, pp. 5394–5409, nov 2019. [Online]. Available: https://ieeexplore.ieee.org/document/8811733/

[23] S. Abeywickrama, R. Zhang, and C. Yuen, "Intelligent Reflecting Surface: Practical Phase Shift Model and Beamforming Optimization," pp. 1–30, 2019. [Online]. Available: http://arxiv.org/abs/1907.06002

[24] Q.-U.-A. Nadeem, A. Kammoun, A. Chaaban, M. Debbah, and M.-S. Alouini, "Intelligent Reflecting Surface Assisted Wireless Communication: Modeling and Channel Estimation," pp. 1–7, 2019. [Online]. Available: http://arxiv.org/abs/1906.02360

[25] Y. Yang, B. Zheng, S. Zhang, and R. Zhang, "Intelligent Reflecting Surface Meets OFDM: Protocol Design and Rate Maximization," pp. 1–32, 2019. [Online]. Available: http://arxiv.org/abs/1906.09956

[26] Y. Yang, S. Zhang, and R. Zhang, "IRS-Enhanced OFDMA: Joint Resource Allocation and Passive Beamforming Optimization," *IEEE Wireless Communications Letters*, pp. 1–1, 2020.

[27] L. Dai, M. D. Renzo, C. B. Chae, L. Hanzo, B. Wang, M. Wang, X. Yang, J. Tan, S. Bi, S. Xu, F. Yang, and Z. Chen, "Reconfigurable Intelligent Surface-Based Wireless Communications: Antenna Design, Prototyping, and Experimental Results," *IEEE Access*, vol. 8, pp. 45 913–45 923, 2020.

[28] Q. Wu and R. Zhang, "Weighted Sum Power Maximization for Intelligent Reflecting Surface Aided SWIPT," *IEEE Wireless Communications Letters*, pp. 1–6, 2019.

[29] Y. Tang, G. Ma, H. Xie, J. Xu, and X. Han, "Joint Transmit and Reflective Beamforming Design for IRS-Assisted Multiuser MISO SWIPT Systems," 2019. [Online]. Available: http://arxiv.org/abs/1910.07156

[30] Q. Wu and R. Zhang, "Joint Active and Passive Beamforming Optimization for Intelligent Reflecting Surface Assisted SWIPT under QoS Constraints," pp. 1–30, 2019. [Online]. Available: http://arxiv.org/abs/1910.06220

[31] C. Pan, H. Ren, K. Wang, M. Elkashlan, A. Nallanathan, J. Wang, and L. Hanzo, "Intelligent Reflecting Surface Aided MIMO Broadcasting for Simultaneous Wireless Information and Power Transfer," pp. 1–33, 2019. [Online]. Available: http://arxiv.org/abs/1908.04863

[32] S. Li, K. Yang, M. Zhou, J. Wu, L. Song, Y. Li, and H. Li, "Full-Duplex Amplify-and-Forward Relaying: Power and Location Optimization," *IEEE Transactions on Vehicular Technology*, vol. 66, no. 9, pp. 8458–8468, 2017.

[33] J. Hagerty, F. Helmbrecht, W. McCalpin, R. Zane, and Z. Popovic, "Recycling Ambient Microwave Energy With Broad-Band Rectenna Arrays," *IEEE Transactions on Microwave Theory and Techniques*, vol. 52, no. 3, pp. 1014–1024, mar 2004. [Online]. Available: http://ieeexplore.ieee.org/document/1273745/

[34] M. Piñuela, P. D. Mitcheson, and S. Lucyszyn, "Ambient RF energy harvesting in urban and semi-urban environments," *IEEE Transactions on Microwave Theory and Techniques*, vol. 61, no. 7, pp. 2715–2726, 2013.

[35] J. P. Curty, N. Joehl, F. Krummenacher, C. Dehollain, and M. J. Declercq, "A model for μ-power rectifier analysis and design," *IEEE Transactions on Circuits and Systems I: Regular Papers*, vol. 52, no. 12, pp. 2771–2779, 2005.

[36] Y. Huang and B. Clerckx, "Large-Scale Multiantenna Multisine Wireless Power Transfer," *IEEE Transactions on Signal Processing*, vol. 65, no. 21, pp. 5812–5827, 2017.

[37] T. Adali and S. Haykin, *Adaptive Signal Processing*. Hoboken, NJ, USA: John Wiley & Sons, Inc., mar 2010. [Online]. Available: http://doi.wiley.com/10.1002/9780470575758

[38] M. C. Grant and S. P. Boyd, "The CVX Users ' Guide, Release 2.0 (beta)," vol. 0, 2013.

[39] Y. Huang and D. P. Palomar, "Rank-constrained separable semidefinite programming with applications to optimal beamforming," *IEEE Transactions on Signal Processing*, vol. 58, no. 2, pp. 664–678, 2010.

[40] S. Boyd, S. J. Kim, L. Vandenberghe, and A. Hassibi, "A tutorial on geometric programming," *Optimization and Engineering*, vol. 8, no. 1, pp. 67–127, 2007.

[41] M. Chiang, *Geometric programming for communication systems*, 2005, vol. 2, no. 1.

[42] B. R. Marks and G. P. Wright, "A General Inner Approximation Algorithm for Nonconvex Mathematical Programs," *Operations Research*, vol. 26, no. 4, pp. 681–683, 1978.

[43] W. C. Li, T. H. Chang, C. Lin, and C. Y. Chi, "Coordinated beamforming for multiuser MISO interference channel under rate outage constraints," *IEEE Transactions on Signal Processing*, vol. 61, no. 5, pp. 1087–1103, 2013.

[44] L. Grippo and M. Sciandrone, "On the convergence of the block nonlinear Gauss-Seidel method under convex constraints," *Operations Research Letters*, vol. 26, no. 3, pp. 127–136, 2000.

[45] M. Hong, M. Razaviyayn, Z. Q. Luo, and J. S. Pang, "A Unified Algorithmic Framework for Block-Structured Optimization Involving Big Data: With applications in machine learning and signal processing," *IEEE Signal Processing Magazine*, vol. 33, no. 1, pp. 57–77, 2016.

[46] Q. Li, M. Hong, H. T. Wai, Y. F. Liu, W. K. Ma, and Z. Q. Luo, "Transmit solutions for MIMO wiretap channels using alternating optimization," *IEEE Journal on Selected Areas in Communications*, vol. 31, no. 9, pp. 1714–1727, 2013.

[47] V. Erceg, L. Schumacher, P. Kyritsi, A. F. Molisch, D. S. Baum, A. Y. Gorokhov, C. Oestges, Q. Li, K. Yu, N. Tal, and B. Dijkstra, "IEEE P802.11 TGn Channel Models," *IEEE 802.11-03/940r4*, no. May, pp. 1–45, 2004.